

A Study of the Multi-frequency Polarization Pulse Profile of Millisecond Pulsars

S. Dai^{1,2}, G. Hobbs¹, R. N. Manchester¹, W. van Straten³, R. Shannon¹, M. Kerr¹

¹CSIRO Astronomy and Space Science, Australia Telescope National Facility, Box 76 Epping NSW 1710, Australia

²Department of Astronomy, School of Physics, Peking University, Beijing 100871, China

³Centre for Astrophysics and Supercomputing, Swinburne University of Technology, PO Box 218, Hawthorn, VIC 3122, Australia

24 July 2014

ABSTRACT

We present high signal-to-noise ratio, multi-frequency polarization profiles for 24 millisecond pulsars that are being observed as a part of the Parkes Pulsar Timing Array (PPTA) project. The pulsars are observed in three bands, centering at ~ 730 MHz, ~ 1400 MHz and ~ 3100 MHz, using the dual-band 10cm/50cm receiver and the central beam of the 20cm multibeam receiver. Data sets that have been well calibrated over several years are utilized, which allows us to study the details and evolution of profiles and show previously undetected profile features. With the high S/N pulse profiles, we show that the overall width of pulse profiles at ~ 1400 MHz increases significantly compared with previous results. 17 of the 24 pulsars show emission over more than half of the pulse period. Both the pulse profile and the position angle variation show complex structures and clear evolutions with frequency. However, the frequency evolution of pulse width is weak, and the frequency evolution of polarization parameters are different from pulsars to pulsars. These results support theories that suggest millisecond pulsar emission regions are wider, at least in terms of pulse longitude, than those of the normal pulsars. The magnetic field of millisecond pulsars could be much more complicated than a dipolar structure.

Key words: pulsars: general

1 INTRODUCTION

Millisecond pulsars (MSPs) are a special subgroup of radio pulsars. Compared with “normal” pulsars, they have much shorter spin periods and smaller spin-down rates, and therefore have larger characteristic ages and weaker implied dipole magnetic fields. On the other hand, the short spin periods and highly stable average pulse shapes of MSPs make them powerful tools to investigate various astrophysical phenomena through the high precision timing (e.g., Manchester 2008).

Although previous studies suggest that MSPs and normal pulsars have similar radiation mechanisms, their emission and polarization properties could be very different. The study of polarization pulse profile of MSPs is then not only important for understanding the pulse emission mechanism, the beaming of pulsar radiation and the geometry of the system, but also crucial for the high precision pulsar timing using MSPs, which relies on the highly stable average profiles.

To date, a number of studies have been carried out focusing on the emission properties of MSPs and presenting

polarization pulse profiles. It has been shown that the spectra of MSPs and normal pulsars are similar (Toscano et al. 1998; Kramer et al. 1998, 1999a), and both of them have high degrees of linear polarization and orthogonal mode position angles (PA) jumps (see e.g., Thorsett & Stinebring 1990; Navarro et al. 1997; Stairs et al. 1999; Manchester & Han 2004; Ord et al. 2004). However, the pulse profiles of MSPs are much more complicated and cover a much larger fraction of the pulse period (Yan et al. 2011b), and the PAs are more complex and do not fit the ‘rotating vector model’ (RVM, Radhakrishnan & Cooke 1969). To explain the complex pulse profiles, multiple emission cones were proposed and discussed by several authors (Rankin 1993; Kramer 1994; Gupta & Gangadhara 2003). An alternative model suggests that the emission beam of a pulsar is filled with randomly distributed emission patches (Lyne & Manchester 1988; Manchester 1995; Han & Manchester 2001). The patchy model may explain more complicated multi-component and asymmetric pulse profiles.

To extend previous studies, the most promising approach is detailed investigations on high signal-to-noise ratio

(S/N), multi-frequency polarization profiles of MSPs. High S/N reveals fine structures and low-level emissions of the pulse profile, and more polarization features, which improve our understanding of the beaming of radiation and emission mechanism. What is more, together with multi-frequency observations, the frequency evolution of both pulse profile and polarization can be investigated. In this paper, we present high S/N, multi-frequency polarization profiles of MSPs, using long PPTA data sets that have been well calibrated. We also present new measurements of flux densities and spectral indice, and polarization parameters.

Details of the observation and data processing are given in Section 2. Multi-frequency polarization profiles of each MSPs are presented in Section 3. In Section 4, we present results of flux densities and spectral indices. In Section 5, the polarization parameters at different frequencies are shown. The implications of the results are discussed in Section 6.

2 OBSERVATIONS AND ANALYSIS

2.1 Observations

We selected observations from the PPTA project, which includes observations of 24 MSPs. The pulsars are observed regularly, with an approximate observing cadence of three weeks, in three bands centred close to 730 MHz, 1400 MHz, and 3100 MHz, using the dual-band 10cm/50cm receiver and the central beam of the 20cm multibeam receiver. In each of the bands, the observing bandwidth was 64 MHz, 256 MHz, and 1024 MHz, respectively. We used both digital polyphase filterbank spectrometers (PDFB4 at 10cm and PDFB3 at 20cm) and coherent dedispersion machines (CASPSR at 50cm). To calibrate the gain and phase of the receiver system, a linearly polarized broad-band and pulsed calibration signal are injected to the two orthogonal linearly polarized probes through a calibration probe at 45° to the signal probes. The pulsed calibration signal was recorded for 2 min prior to each pulsar observation. Signal amplitudes were placed on a flux density scale using observations of Hydra A. All data were recorded using the PSRFITS data format (Hotan et al. 2004) with 1-min subintegrations and the full spectral resolution. (for futher details see Manchester et al. (2013), and references therein).

Most of the pulsars in the sample show large flux variability at the PPTA observing frequencies due to diffractive and refractive scintillation. We find that for some of the pulsars in the PPTA sample show measured intensities > 20 times of the mean; for these observations, Parkes observations can have S/N in excess of larger aperture telescopes such as the Green Bank Telescope and represent average observation with the MeerKAT telescope.

2.2 Analysis

The data were processed using the PSRCHIVE software package (Hotan et al. 2004). To excise radio-frequency interference, we median-filtered each sub-integration and remove 5 per cent of each edge of the bandpass. The polarization was then calibrated by correcting for differential gain and phase between the receptors using associated calibration files. For 20cm observations with the Multibeam receiver,

we corrected for cross coupling between the feeds through a mode derived from an observation of PSR J0437–4715 that covered a wide range of parallactic angles.

The Stokes parameters were in accordance with the astronomical conventions described by van Straten et al. (2010). Stokes V is defined as $I_{\text{LH}} - I_{\text{RH}}$, using the IEEE definition for sense of circular polarization. Stokes L was calculated as $L = (Q^2 + U^2)^{1/2}$, and the noise bias in L was corrected according to Lorimer & Kramer (2005), and the similar bias in V was corrected as described in Yan et al. (2011b). PAs were calculated as $\psi = 0.5 \tan^{-1}(U/Q)$, which are absolute and measured from celestial north towards east, i.e. counterclockwise on the sky. The error of PA was estimated according to Everett & Weisberg (2001), and the PA curve is plotted only when the linear polarization is greater than 4σ . The baseline region was computed for all four Stokes-parameter profiles, separately, and baselines for each of the Stokes parameter profiles were set to zero mean.

In order to add the data in time to form a final mean profile, pulse times of arrival were obtained for each observation using an analytic template based on an existing high S/N pulse profile. The TEMPO2 pulsar timing package (Hobbs et al. 2006) was then used to fit pulsar spin, astrometric and binary parameters, and also fit harmonic waves if necessary to give white timing residuals for each pulsar. Finally, the separate observations were summed using this timing model to determine relative phases and form the final Stokes-parameter profiles. To give the best possible S/N in the final profile, the individual observation profiles were weighted by their $(S/N)^2$ when forming the sum profile.

To form mean polarization profiles, the Faraday rotation across the band should be corrected. According to Yan et al. (2011a), the interstellar rotation measure (RM) of PPTA MSPs are stable, and we used interstellar RM values from Yan et al. (2011b). To account for the contribution of the Earth's ionosphere, we used two ionospheric models, the International Reference Ionosphere (IRI) model suggested in Yan et al. 2011b and the IonFR model used by Sotomayor-Beltran et al. (2013). We found that the ionospheric RM value from the above two models for a particular observation of one pulsar could be significantly different at some epoches. By comparing PAs between 50cm observations at different epoches corrected using these two models, respectively, we found that the IRI model was more self-consistent. This might be due to the insufficient coverage of the Global Positioning System (GPS) in the southern hemisphere, based on which the IonFR model works. Therefore, we calculated and corrected the ionospheric RM contributions using IRI models through our analysis.

In Table 1, we summarize the observational parameters for the 25 PPTA pulsars which were observed. Other basic pulsar parameters can be obtained from the ATNF Pulsar Catalogue (Manchester et al. 2005). For each band of the pulsars, we present the band width, the number of frequency channels across the band and the number of bins across the pulse period. The dispersion smearing across each frequency channel is calculated according to,

$$\Delta t_{\text{DM}} \approx 8.30 \times 10^6 \text{ DM } \Delta f \text{ } f^{-3} \text{ ms}, \quad (1)$$

and is given in units of profile bins. Δf is the channel width in MHz, f is the band centre frequency in MHz, and the DM is in units of $\text{cm}^{-3} \text{ pc}$. We also estimate the pulse broadening

time due to scattering using the empirical fit from Bhat et al. (2004),

$$\log \tau_d = -6.46 + 0.154 \log \text{DM} + 1.07(\log \text{DM})^2 - (3.86 \pm 0.16) \log \nu, \quad (2)$$

where ν is the band centre frequency in GHz. The last two columns give the number of observations summed and the total observation times.

3 MULTI-FREQUENCY POLARIZATION PROFILES

In this section, we present the multi-frequency polarization profiles for the 24 PPTA MSPs. PA variations and polarization profiles in all three bands for each MSP are shown, with the baseline details presented in the bottom panel of each figure. In Table 2, we present the overall pulse width and pulse widths at 50 per cent of the peak flux density (W50) and 10 per cent of the peak (W10), all in degrees of longitude, where 360 is equivalent to the pulse period or 1.0 in pulse phase, and in milliseconds. The overall pulse width is measured from the first point to the last point where the pulse intensity significantly exceeds the baseline noise Yan et al. (2011b), with pulse profiles in the 20 cm band since they normally have the highest S/N. In Fig. 1, the W10 and W50 are plotted against frequency for each MSP.

Compared with previous studies, we have obtained much higher S/N for polarization pulse profiles in the 728 MHz, 1369 MHz and 3100 MHz. We find new low-level emissions for PSR J2145–0750. We also show much more details of the PA curves. We show clear frequency evolution of pulse profiles.

In the following subsections, we present and discuss the multi-frequency polarization profile of each MSPs.

3.1 PSR J0437–4715

The top panel of Fig. 2 shows the polarization pulse profiles of the strongest PPTA MSP, PSR J0437–4715, in three bands. At 1369 MHz, our results are in good agreement with previously published works (Johnston et al. 1993; Manchester & Johnston 1995; Navarro et al. 1997; Yan et al. 2011b), which present multiple overlapping components and complex polarization variations across the pulse profile. The profile of total intensity shows clear frequency development. As the frequency decreases, both the leading and trailing emissions becomes stronger. At lower frequencies, the main pulse split into two peaks and the second peak becomes stronger than the first peak. The PA curves change dramatically in different bands. While the orthogonal transition close to the main profile peak exists in all three bands, previously reported non-orthogonal transitions at 1369 MHz disappear in other two bands, and new transitions and discontinuous features can be observed at 728 MHz and 3100 MHz bands.

3.2 PSR J0613–0200

The middle panel of Fig. 2 shows the polarization pulse profiles of PSR J0613–0200, in three bands. At 1369 MHz, our

results are in good agreement with previously published results (Ord et al. 2004; Yan et al. 2011b). Our high S/N profiles provide more details in the PA curve, and we show that the PA curves are complex and very different in three bands. At 1369 MHz, the discontinuous PA at the leading edge of the trailing component reported by Yan et al. (2011b) are not observed, and the PA curve seems to be continuous. The main pulse of the profile shows clear frequency evolution, and most significantly, the trailing peak becomes much stronger at low frequencies relative to the rest of the profile and split into two peaks as previously observed by Stairs et al. (1999). From the high frequencies to low frequencies, the fractional linear polarization increases, and the trailing component becomes high linear polarized.

3.3 PSR J0711–6830

The bottom panel of Fig. 2 shows the polarization pulse profiles of PSR J0711–6830, in three bands. At 1369 MHz, our results are in good agreement with previously published results (Ord et al. 2004; Yan et al. 2011b). The double-peak weak component following the second peak is clear. The orthogonal mode transition after the peak of the leading component is confirmed, and possible orthogonal mode transitions at the trailing edge of the main peak are observed at 1369 MHz and disappear at lower frequencies. Except for that at lower frequencies, the leading component becomes stronger relative to the main pulse and the fractional linear polarization of the main peak increase significantly, the frequency evolution of the profile is not significant.

3.4 PSR J1017–7156

The top panel of Fig. 3 shows the polarization pulse profiles of PSR J1017–7156, in three bands. Our results are in good agreement with and extend previously published results (Keith et al. 2012). We show that the PA variations are more complex than was observed in previous work. Both the linear and circular polarisation shows significant evolution with frequency, and the trailing emission becomes stronger at higher frequencies.

3.5 PSR J1022+1001

The middle panel of Fig. 3 shows the polarization pulse profiles of PSR J1022+1001, in three bands. Our results are in good agreement with previously published results (Kramer et al. 1999b; Stairs et al. 1999; Ord et al. 2004; Yan et al. 2011b). The PA variation generally fits the RVM in all three bands, but near the centre of the profile, it is discontinuous in the 10cm bands and shows glitch in the 20cm and 50cm bands as reported by Yan et al. (2011b). The relative strength of the two main peaks evolves dramatically with frequency. While the second peak keeps highly linear polarized, the first peak depolarizes rapidly.

3.6 PSR J1024–0719

The bottom panel of Fig. 3 shows the polarization pulse profiles of PSR J1024–0719, in three bands. At 1369 MHz, our results are in good agreement with previously published

Table 1. Observational parameters for the 25 PPTA MSPs.

PSR	Frequency (MHz)	Band width (MHz)	No. of channels	No. of bins	DM smear (bins)	τ_d (bins)	No. of obs.	Integration time (h)
J0437–4715	730	64	256	1024	7.9	0.0	177	142.9
	1400	256	1024	1024	0.4	0.0	669	502.2
	3100	1024	1024	2048	0.3	0.0	281	248.8
J0613–0200	730	64	256	1024	218.0	0.3	64	66.0
	1400	256	1024	512	5.2	0.02	160	159.3
	3100	1024	1024	512	1.8	0.0	111	113.9
J0711–6830	730	64	256	1024	57.7	0.02	72	65.9
	1400	256	1024	1024	2.8	0.0	161	161.1
	3100	1024	1024	1024	1.0	0.0	102	102.2
J1017–7156	730	64	256	1024	693.4	15.4	85	86.5
	1400	256	2048	256	4.2	0.3	135	130.4
	3100	1024	2048	512	2.9	0.03	73	76.3
J1022+1001	730	64	256	1024	10.7	0.0	65	58.4
	1400	256	1024	2048	1.0	0.0	148	138.3
	3100	1024	1024	2048	0.4	0.0	117	110.5
J1024–0719	730	64	256	1024	21.6	0.0	34	36.1
	1400	256	1024	1024	1.0	0.0	112	111.0
	3100	1024	1024	1024	0.4	0.0	59	61.5
J1045–4509	730	64	256	1024	133.9	0.6	63	42.7
	1400	256	2048	512	1.6	0.03	137	138.9
	3100	1024	1024	1024	2.2	0.0	103	104.5
J1446–4701	730	64	256	1024	437.8	1.9	19	15.2
	1400	256	512	512	21.1	0.08	50	39.4
	3100	1024	1024	1024	7.3	0.01	9	8.8
J1545–4550	730	64	256	1024	329.2	2.6	15	13.2
	1400	256	1024	512	7.9	0.1	21	20.6
	3100	1024	1024	1024	5.5	0.01	15	12.2
J1600–3053	730	64	256	1024	250.3	0.9	53	56.6
	1400	256	1024	512	6.0	0.04	139	129.9
	3100	1024	1024	512	2.1	0.0	106	108.0
J1603–7202	730	64	256	1024	44.1	0.07	52	44.4
	1400	256	2048	1024	1.1	0.01	131	127.4
	3100	1024	1024	1024	0.7	0.0	49	50.6
J1643–1224	730	64	256	1024	232.4	1.4	53	53.7
	1400	256	2048	512	2.8	0.06	116	117.0
	3100	1024	1024	1024	3.9	0.01	93	93.4
J1713+0747	730	64	256	1024	60.2	0.01	66	67.8
	1400	256	1024	1024	2.9	0.0	155	132.0
	3100	1024	1024	1024	1.0	0.0	110	107.9
J1730–2304	730	64	256	1024	20.4	0.0	57	51.0
	1400	256	1024	1024	1.0	0.0	104	105.8
	3100	1024	1024	2048	0.7	0.0	62	62.2
J1744–1134	730	64	256	1024	13.3	0.0	65	66.0
	1400	256	512	1024	1.3	0.0	129	126.7
	3100	1024	1024	1024	0.2	0.0	96	99.5
J1824–2453	730	64	256	1024	675.5	34.8	33	33.0
	1400	256	2048	256	4.1	0.8	88	82.9
	3100	1024	1024	512	5.6	0.06	54	53.6
J1832–0836	730	64	256	1024	178.3	0.1	12	9.0
	1400	256	1024	512	4.3	0.01	19	16.9
	3100	1024	1024	1024	3.0	0.0	11	10.1
J1857+0943	730	64	256	1024	42.7	0.01	54	27.8
	1400	256	1024	1024	2.1	0.0	99	50.9
	3100	1024	1024	1024	0.7	0.0	68	35.5
J1909–3744	730	64	256	1024	60.7	0.01	95	91.3
	1400	256	1024	512	1.5	0.0	218	191.1
	3100	1024	1024	1024	1.0	0.0	138	129.4

Table 1. Continued.

PSR	Frequency (MHz)	Band width (MHz)	No. of channels	No. of bins	DM smear (bins)	τ_d (bins)	No. of obs.	Integration time (h)
J1939+2134	730	64	256	512	392.3	3.5	58	26.4
	1400	256	1024	256	9.4	0.2	102	49.4
	3100	1024	1024	256	3.3	0.01	91	46.0
J2124-3358	730	64	256	1024	16.0	0.0	40	20.3
	1400	256	1024	1024	0.8	0.0	134	68.5
	3100	1024	1024	1024	0.3	0.0	78	40.5
J2129-5721	730	64	256	1024	147.1	0.1	59	31.1
	1400	256	1024	512	3.5	0.01	116	112.6
	3100	1024	1024	512	1.2	0.0	17	9.0
J2145-0750	730	64	256	1024	9.7	0.0	70	65.1
	1400	256	1024	2048	0.9	0.0	134	129.3
	3100	1024	1024	2048	0.3	0.0	117	111.2
J2241-5236	730	64	256	1024	89.8	0.01	75	69.8
	1400	256	1024	512	2.1	0.0	188	152.3
	3100	1024	1024	1024	1.5	0.0	93	92.9

Table 2. Pulse width for PPTA MSPs.

PSR	Overall width		W_{10}		W_{50}		
	1400 MHz (deg)	730 MHz (deg)	1400 MHz (deg)	3100 MHz (deg)	730 MHz (deg)	1400 MHz (deg)	3100 MHz (deg)
J0437-4715	299.5	130.5	63.4	18.6	15.4	8.9	5.6
J0613-0200	178.2	105.9	109.1	105.4	10.5	54.9	30.4
J0711-6830	283.3	180.9	168.2	167.8	131.4	124.3	108.7
J1017-7156	70.6	22.2	21.7	34.4	16.1	10.7	11.0
J1022+1001	72.1	41.9	43.0	35.8	16.5	21.1	8.2
J1024-0719	277.7	123.6	109.6	113.7	67.3	35.7	32.0
J1045-4509	357.9	70.3	69.7	66.6	33.5	36.6	35.7
J1446-4701	93.0		45.2			12.2	
J1545-4550	243.8		56.8			12.8	
J1600-3053	77.5	48.6	41.3	42.1	11.2	9.3	22.7
J1603-7202	239.3	48.3	41.8	38.5	32.4	29.4	7.0
J1643-1224	231.8	83.8	72.6	65.7	32.8	24.9	20.5
J1713+0747	131.3	42.3	30.3	29.6	16.4	8.8	8.3
J1730-2304	247.7	68.9	76.0	73.0	34.2	43.2	43.8
J1732-5049							
J1744-1134	204.1	24.0	21.9	20.1	13.1	12.3	8.8
J1824-2452	269.6	219.1	191.0	170.0	113.4	115.4	7.7
J1832-0836	285.3		244.1			113.2	
J1857+0943	358.3	219.0	202.4	203.4	42.4	35.2	31.2
J1909-3744	189.5	13.1	11.0	9.2	6.9	5.3	4.3
J1939+2134	355.8	207.0	199.3	204.5	195.1	182.1	10.5
J2124-3358	358.9		269.7	282.9		37.5	31.8
J2129-5721	159.2	37.5	60.0	88.4	22.9	25.5	53.8
J2145-0750	277.3	94.1	93.6	91.1	9.1	7.6	7.8
J2241-5236	221.2	18.8	20.3	21.0	10.3	10.6	9.8

results (Ord et al. 2004; Yan et al. 2011b). Besides the flat PA curve across the main part of the profile as previously reported, we also show the PAs of the trailing component which varies across the profile. From high frequencies to low frequencies, the leading component and the trailing component of the profile become relatively stronger and the peak just after the main peak becomes weaker.

3.7 PSR J1045-4509

The top panel of Fig. 4 shows the polarization pulse profiles of PSR J1045-4509, in three bands. At 1369 MHz, our results are in good agreement with previously published results (Yan et al. 2011b), and confirm the leading emission which is joined to the main pulse by a low-level bridge of

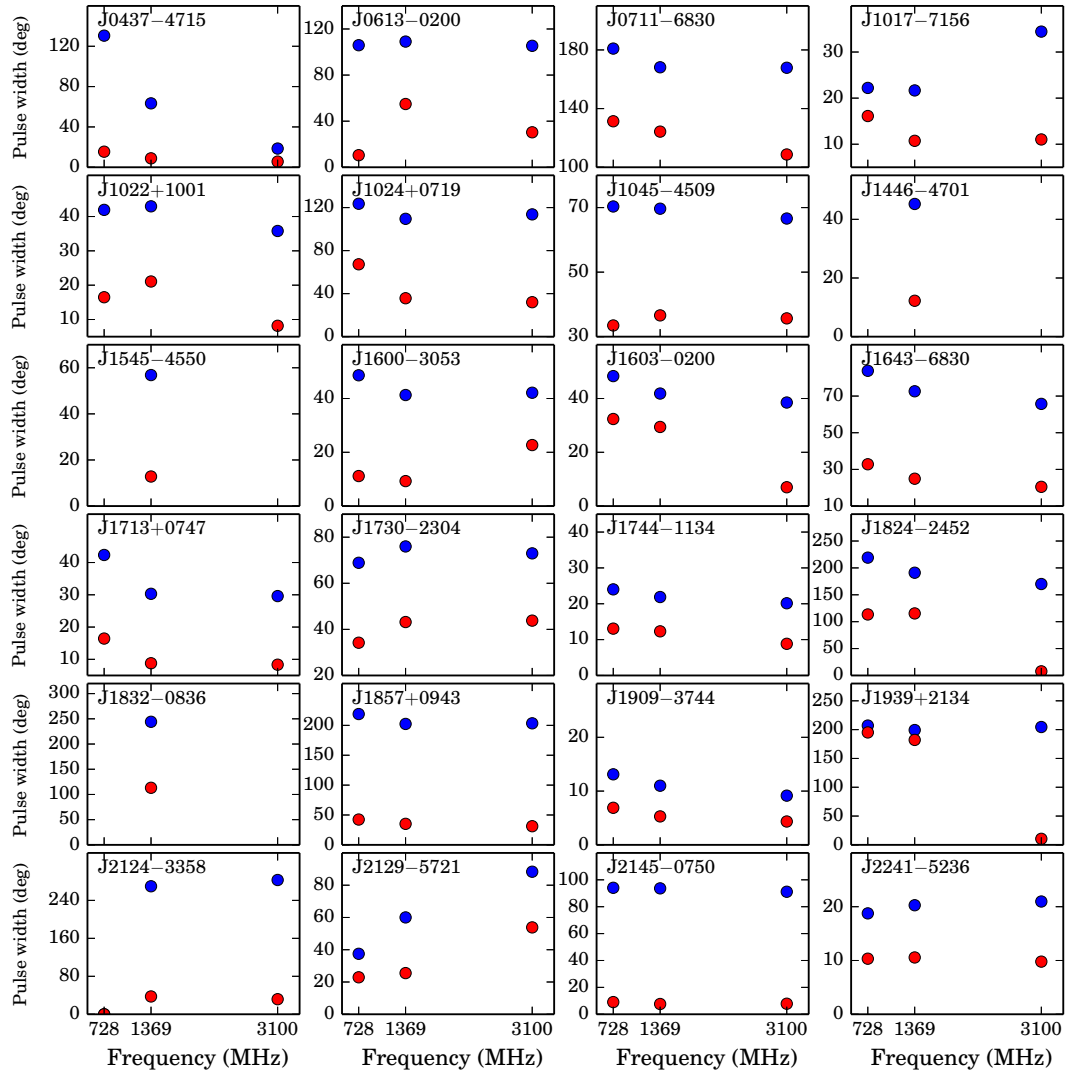


Figure 1. Pulse widths at 10 and 50 per cent of the peak flux density, both in degrees of longitude. Red and blue points represent W10 and W50, respectively.

emission. We show the complex PA curve with more details, especially the PA of the low-level bridge connecting the leading emission and the main pulse. At the leading edge of the main pulse, there is a non-orthogonal transition rather than a orthogonal transition expected by citet{Yan11}. Except for that at low frequencies, the peak at the trailing edge of the

main peak disappears and the fractional linear polarization of the trailing emission decreases, the profile evolution is not significant.

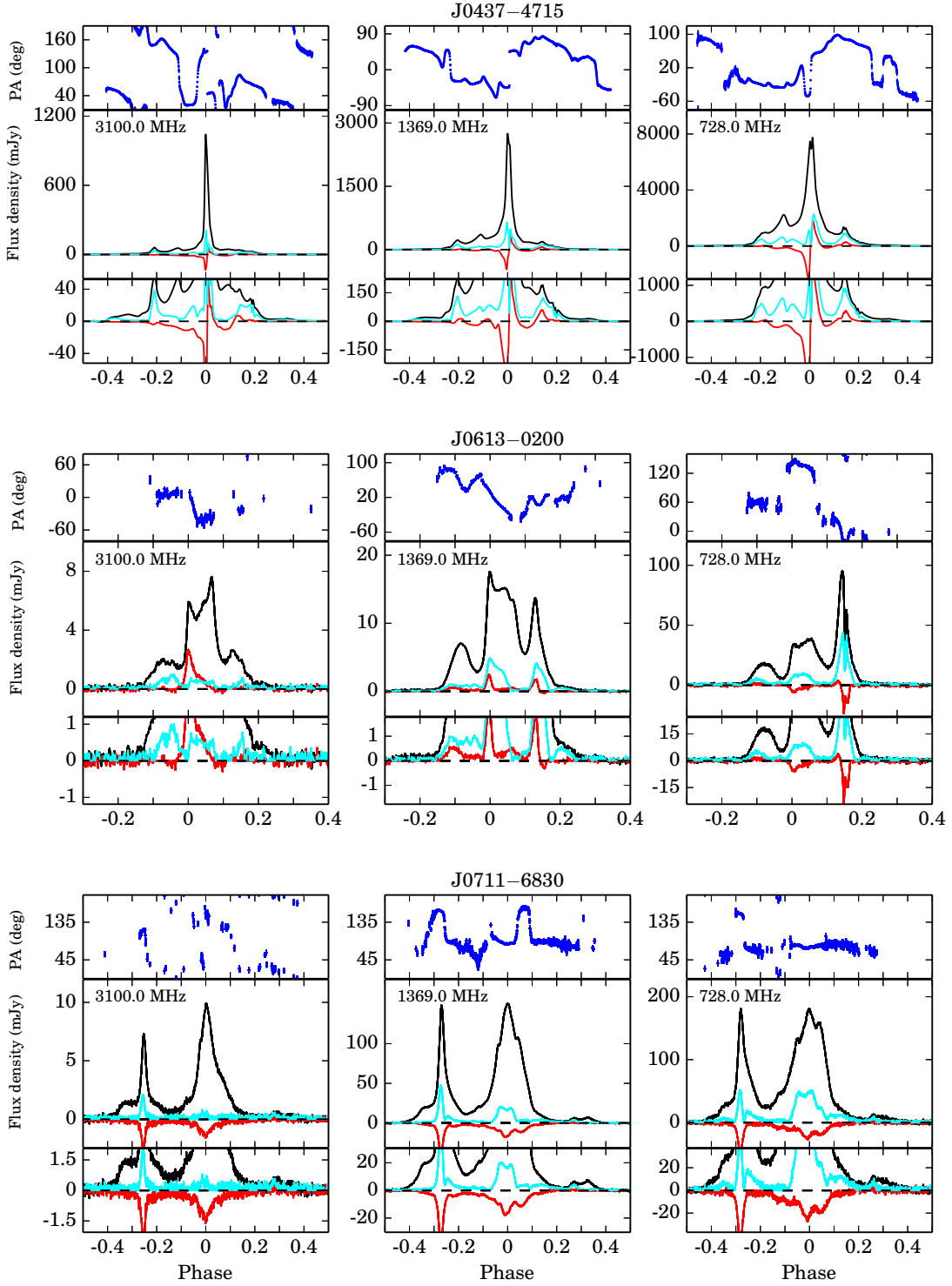


Figure 2. Multi-frequency polarization profiles for PSR J0437–4715 (top panel), PSR J0613–0200 (middle panel) and PSR J0711–6830 (bottom panel). The upper part of each panel gives the PA of the linearly polarized emission. The middle part presents the pulse profile for the total intensity I (thick solid line), linearly polarized intensity L (blue thin line) and circularly polarized intensity (red thin line), and the lower part shows the low-level details of the polarization profiles.

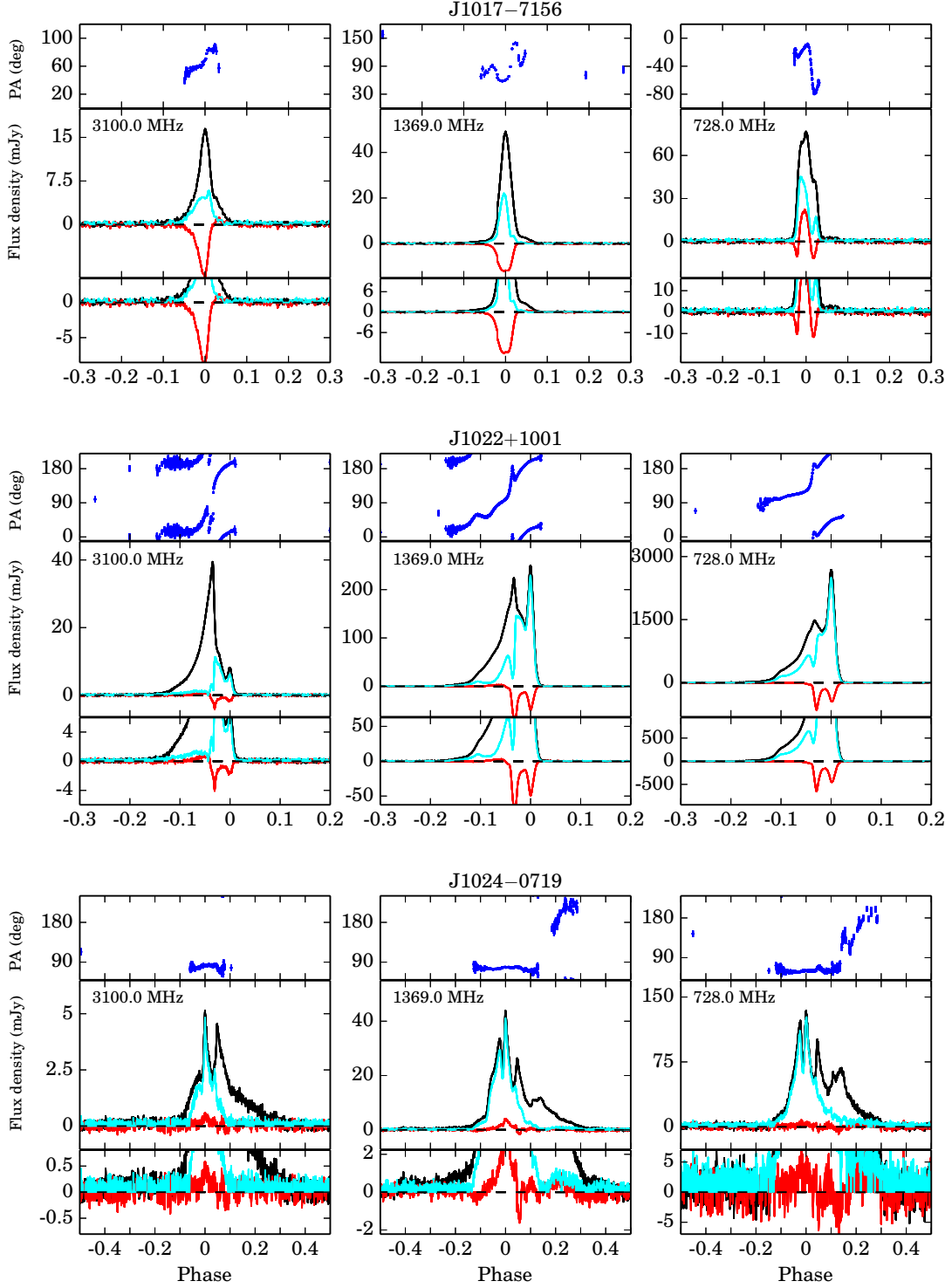


Figure 3. Multi-frequency polarization profiles for PSR J1017–7156 (top panel), PSR J1022+1001 (middle panel) and PSR J1024–0719 (bottom panel). See Fig. 2 for further details.

3.8 PSR J1446–4701

The middle panel of Fig. 4 shows the polarization pulse profiles of PSR J1446–4701, in three bands. At 1369 MHz, our results are generally consistent with previously published results (Keith et al. 2012). The PAs are flat over the main

pulse, but show variations over the leading and trailing emissions.

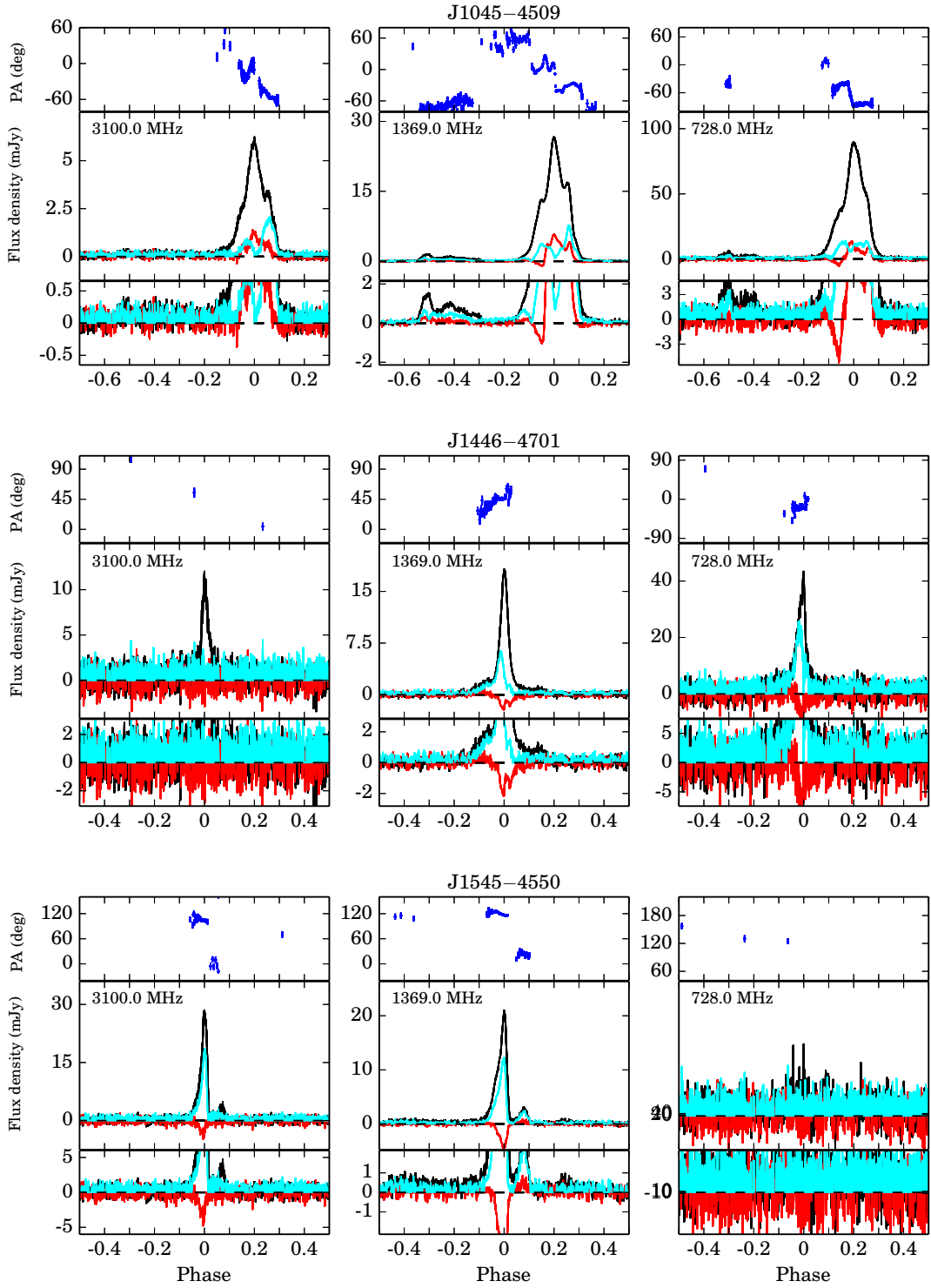


Figure 4. Multi-frequency polarization profiles for PSR J1045–4509 (top panel), PSR J1446–4701 (middle panel) and PSR J1545–4550 (bottom panel). See Fig. 2 for further details.

3.9 PSR J1545–4550

The bottom panel of Fig. 4 shows the polarization pulse profiles of PSR J1545–4550, in three bands. At 1369 MHz, Burgay et al. (2013) shows an component around phase 0.35 that we do not see in our analysis. We have confirmed with the

HTRU collaboration that this extra component was caused by an error in their analysis. Apart from this, our profiles are consistent in all three frequency bands. We also show that the low-level emissions could extend over at least 80 per cent of the pulse period.

3.10 PSR J1600–3053

The top panel of Fig. 5 shows the polarization pulse profiles of PSR J1600–3053, in three bands. At 1369 MHz, our results are generally consistent with previously published results (Ord et al. 2004; Yan et al. 2011b). The fractional linear polarization decreases at lower frequencies.

3.11 J1603–7202

The middle panel of Fig. 5 shows the polarization pulse profiles of J1603–7202, in three bands. At 1369 MHz, our results are in good agreement with previously published results (Ord et al. 2004; Yan et al. 2011b). The broad low-level feature preceding the main pulse and the double-peak trailing pulse can be clearly identified. We find that there are low-level emissions connecting the main pulse and the double-peak trailing pulse. As frequency decreases, the second peak of the mean pulse profile becomes highly circular polarized, and the PAs between two main peaks show great changes.

3.12 J1643–1224

The bottom panel of Fig. 5 shows the polarization pulse profiles of J1643–1224, in three bands. At 1369 MHz, our results are in good agreement with and extend previously published results (Ord et al. 2004; Yan et al. 2011b). The PA of the broad feature preceding the main pulse is determined and found to be discontinuous with the rest of the PA variation. Both the linear and circular polarization develop with frequency.

3.13 J1713+0747

The top panel of Fig. 6 shows the polarization pulse profiles of J1713+0747 in three bands. At 1369 MHz, our results are consistent with previously published results (Ord et al. 2004; Yan et al. 2011b), showing the almost complete linear polarized leading and trailing components. At 3100 MHz, one orthogonal PA transition at the leading edge of the main peak is observed. At 1369 MHz, a new orthogonal PA transition at around phase 0.02 appears. At 728 MHz, another orthogonal PA transition appears at phase 0.9.

3.14 J1730–2304

The middle panel of Fig. 6 shows the polarization pulse profiles of J1730–2304 in three bands. At 1369 MHz, our results are consistent with previously published results (Ord et al. 2004; Yan et al. 2011b), clearly showing the weak leading and trailing components.

3.15 J1744–1134

The bottom panel of Fig. 6 shows the polarization pulse profiles of J1744–1134 in three bands. At 1369 MHz, our results are consistent with previously published results (Yan et al. 2011b). The multiple-component precursor is clearly identified and no significant post-cursor component is observed. The PA of the precursor is shown and seems to be complex

but continuous. The circular polarization grows stronger from 3100 to 1369 MHz, but diminish at 728 MHz.

3.16 J1824–2452

The top panel of Fig. 7 shows the polarization pulse profiles of J1824–2452 in three bands. At 1369 MHz, our results are consistent with and extend previously published results (Yan et al. 2011b). The highly linear polarized component leading the first peak and its PA are shown. The PA variation across these components appears continuous.

3.17 J1832–0836

The middle panel of Fig. 7 shows the polarization pulse profiles of J1832–0836 in three bands. At 1369 MHz, our results are consistent with and extend previously published results (Burgay et al. 2013). The components around phase -0.45 and -0.08 are highly linearly polarized. The PAs around phase -0.05 and 0.3 show evidences of jumps, but is hard to confirm due to the low S/N.

3.18 J1857+0943

The bottom panel of Fig. 7 shows the polarization pulse profiles of J1857+0943 in three bands. At 1369 MHz, our results are generally consistent with previously published results (Yan et al. 2011b). We show more details of the PA variation, which is very complex and inconsistent with the RVM.

3.19 J1909–3744

The top panel of Fig. 8 shows the polarization pulse profiles of J1909–3744 in three bands. At 1369 MHz, our results are generally consistent with results of Ord et al. (2004); Yan et al. (2011b), showing a narrow main pulse and a weak feature preceding the main pulse by about 0.45 in phase. The fractional linear polarization increases as the frequency decreases, and the PAs do not change much across bands.

3.20 J1939+2134

The middle panel of Fig. 8 shows the polarization pulse profiles of J1939+2134 in three bands. At 1369 MHz, our results are generally consistent with previously published results (Yan et al. 2011b). As explained in Yan et al. (2011b), because of the high DM/P , our observations are significantly affected by DM smearing, and we do not see the secondary maxima at the trailing edges of both the main pulses and interpulse (Thorsett & Stinebring 1990; Stairs et al. 1999; Ord et al. 2004). We confirmed the existence of weak components preceding both the main pulse and interpulse in all three bands, and rule out the possibility of undetected RFI or instrumental problems. Our results show stronger left-circular emission in the main pulse compared to (Yan et al. 2011b). The fractional linear polarization of the main pulse increases significantly as frequency decreases while that of the interpulse decreases.

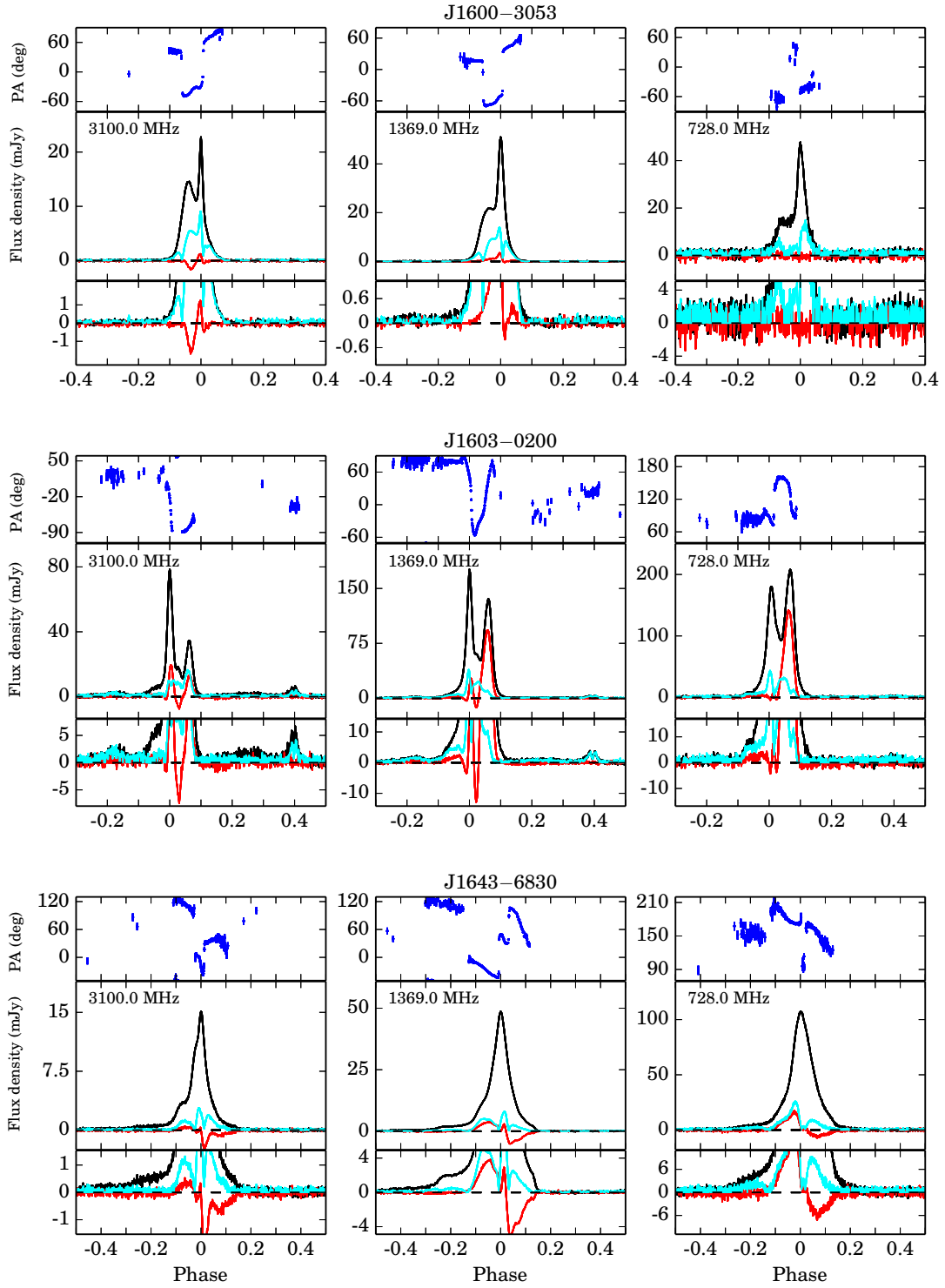


Figure 5. Multi-frequency polarization profiles for PSR J1600–3053 (top panel), PSR J1603–7202 (middle panel) and PSR J1643–1224 (bottom panel). See Fig. 2 for further details.

3.21 J2124–3358

The bottom panel of Fig. 8 shows the polarization pulse profiles of J2124–3358 in three bands. At 1369 MHz, the complex profile we show here is generally consistent with previously published results (Yan et al. 2011b). We are able

to provide more details of the PA variation and show that it has complex structures. The fractional linear polarization of the main pulse increases at lower frequencies.

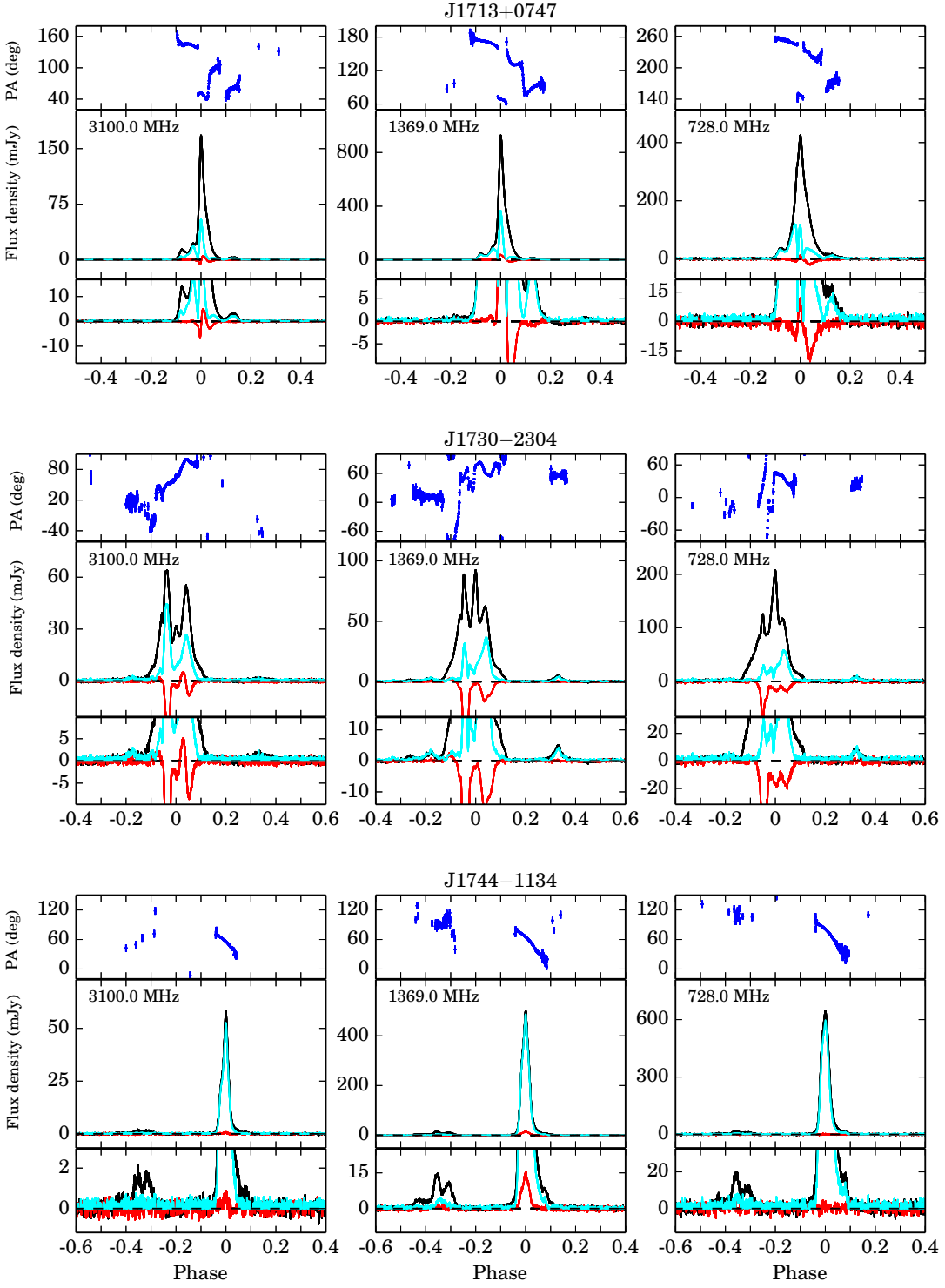


Figure 6. Multi-frequency polarization profiles for PSR J1713+0747 (top panel), PSR J1730–2304 (middle panel) and PSR J1744–1134 (bottom panel). See Fig. 2 for further details.

3.22 J2129–5721

The top panel of Fig. 9 shows the polarization pulse profiles of J2124–5721 in three bands. At 1369 MHz, our results are in good agreement with and extend previously published results (Yan et al. 2011b). The weaker leading shelf of emis-

sion extends to at least phase of −0.4, and the post-cursor clearly has multiple components. We show more details of PA in the trailing edge of the main pulse, and show that PA do not simply decrease through the pulse, and discontinuous features at the phase of the trailing main-pulse component

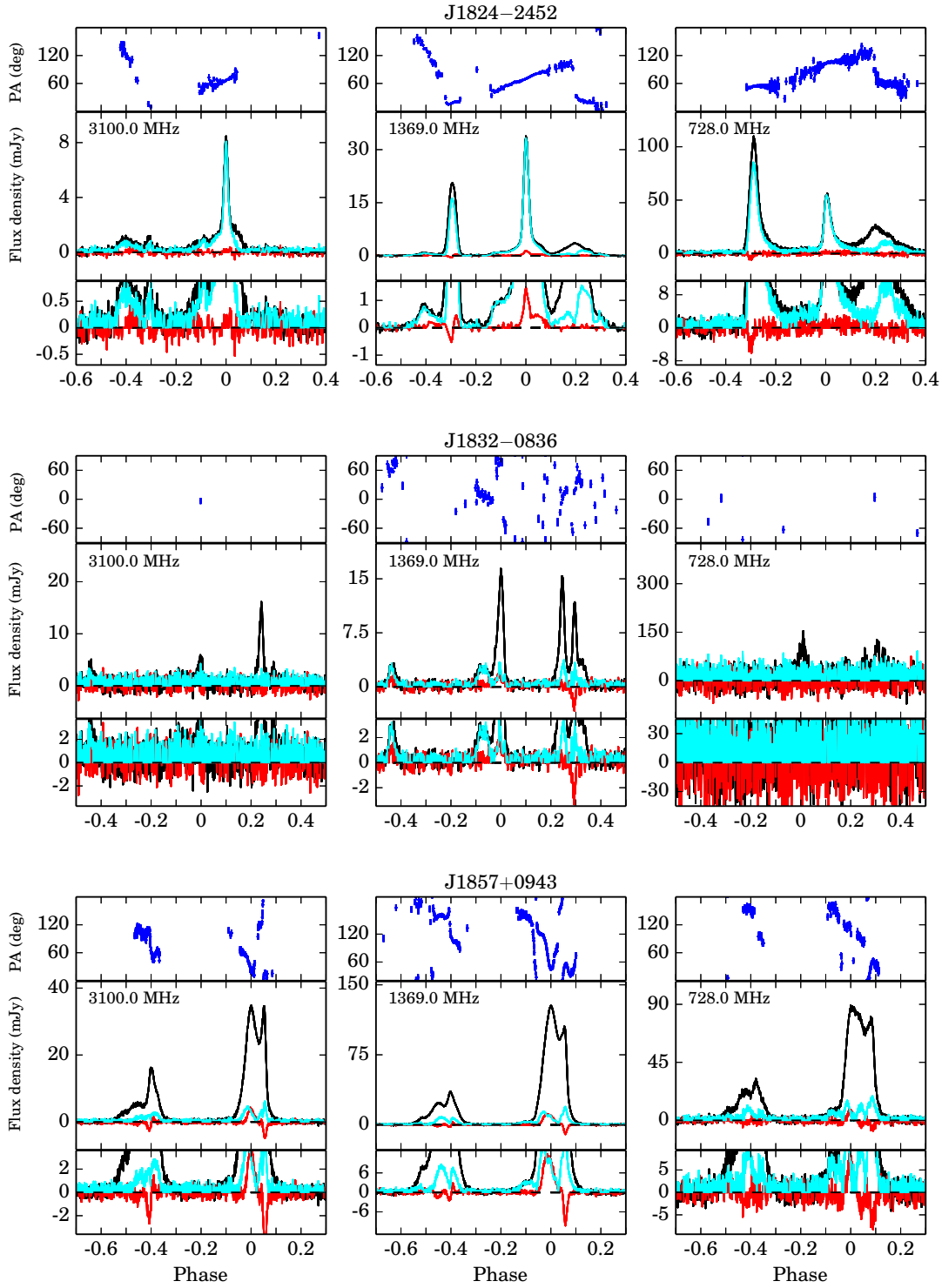


Figure 7. Multi-frequency polarization profiles for PSR J1824–2452 (top panel), PSR J1832–0836 (middle panel) and PSR J1857+0943 (bottom panel). See Fig. 2 for further details.

are confirmed. The fractional linear polarization of the main pulse increases as frequency decreases.

3.23 J2145–0750

The middle panel of Fig. 9 shows the polarization pulse profiles of J2145–0750 in three bands. At 1369 MHz, our results are in good agreement with and extend previously published results (Yan et al. 2011b). A new orthogonal transition ap-

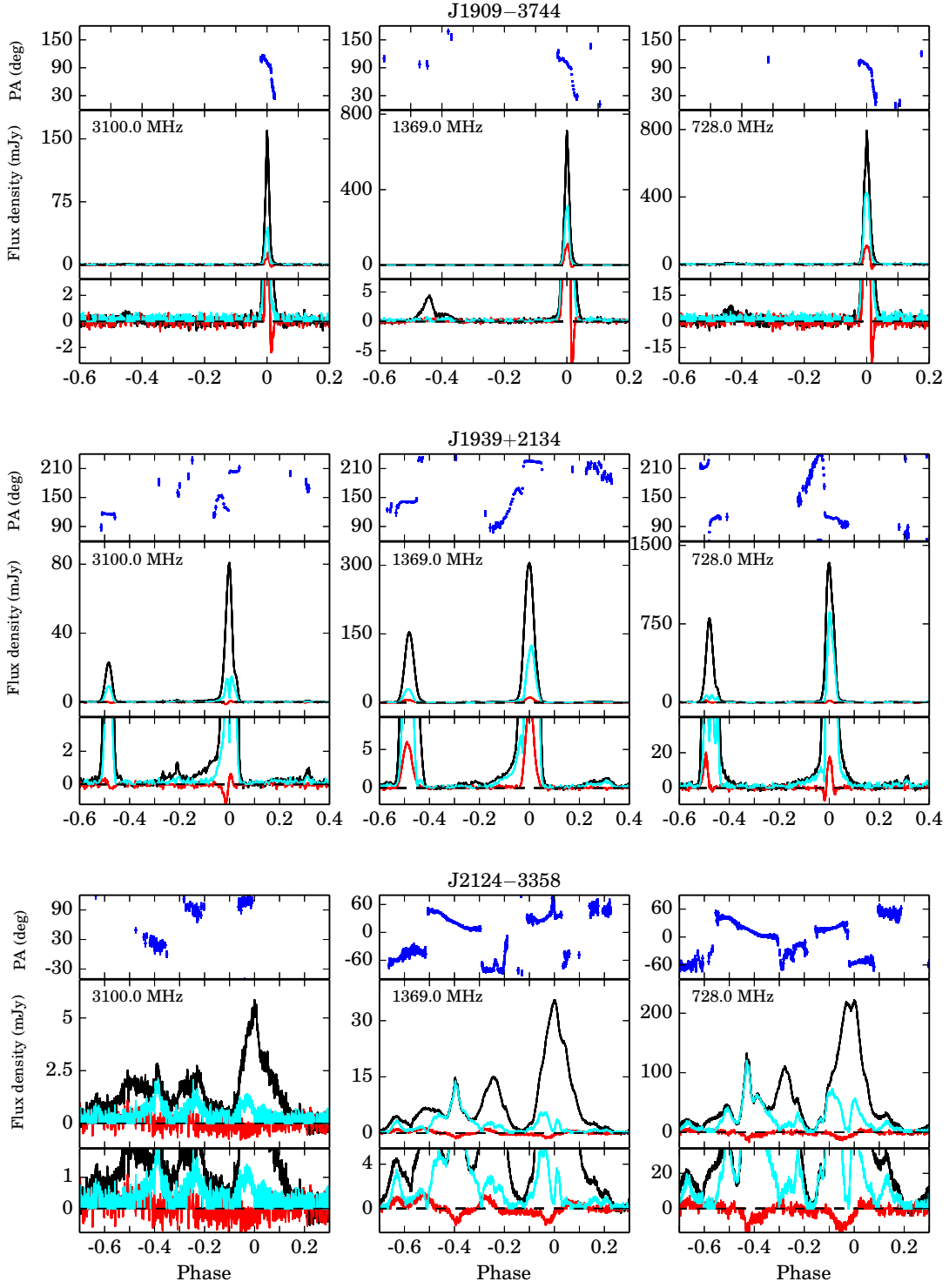


Figure 8. Multi-frequency polarization profiles for PSR J1909–3744 (top panel), PSR J1939+2134 (middle panel) and PSR J2124–3358 (bottom panel). See Fig. 2 for further details.

pears at the trailing edge of the main peak in the 50cm band. Around phase 0.4, there are evidences of low-level emissions which significantly extends the overall width of this MSPs.

3.24 J2241–5236

The bottom panel of Fig. 9 shows the polarization pulse profiles of J2241–5236 in three bands. At 1369 MHz, our results generally agree with and extend previously published results (Keith et al. 2011). We show a new low-level compo-

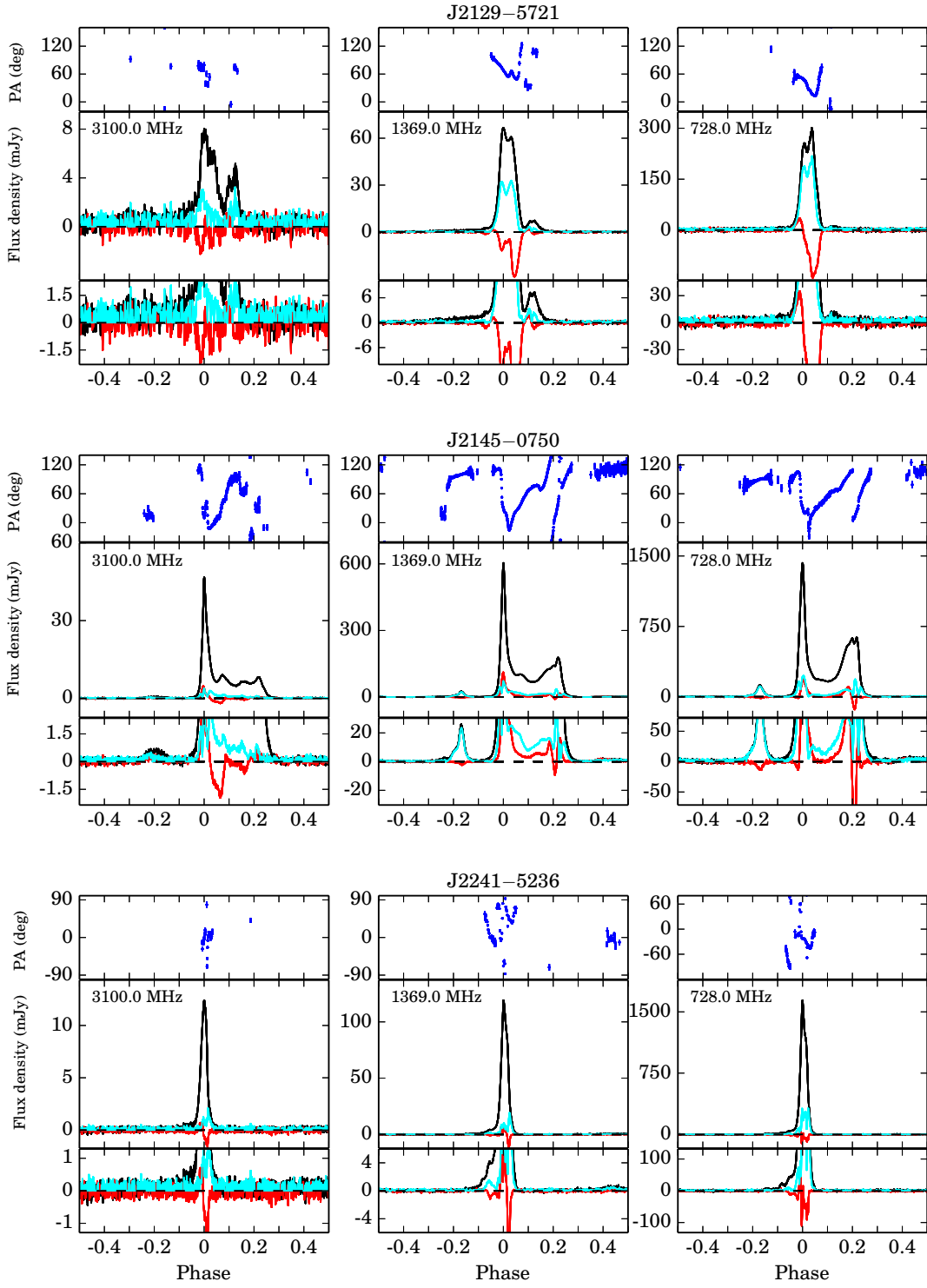


Figure 9. Multi-frequency polarization profiles for PSR J2129–5721 (top panel), PSR J2145–0750 (middle panel) and PSR J2241–5236 (bottom panel). See Fig. 2 for further details.

ment around phase 0.4 with a width of ~ 0.2 . We also show more details of the PA variations which are complex and discontinuous.

4 FLUX DENSITIES AND SPECTRAL INDICES

In Table 3, we present the flux densities and spectral indices for all MSPs. Firstly, the mean flux density $S = \langle I \rangle$ of three bands averaged over all observations and its uncer-

tainty are given. Then, the root mean square (rms) fluctuation in individual-observation flux densities are presented. Finally, we show the spectral indices. In Fig. 10, the flux densities are plotted against frequency for each MSPs.

Compared with Yan et al. (2011b), the mean flux densities of several MSPs in the 20 cm band show significant differences, which is caused by interstellar scintillation effects. Although we are averaging over a much longer time-span and a larger number of observations, we find that measurements of flux densities could still be biased by diffractive scintillations and the distributions of flux density are clearly non-gaussian. From Fig. 10, we can see that a single power-law can fit the spectra of most MSPs. Exceptions are PSR J1600–3053 and PSR J1713+0747, whose spectra show flattening at lower frequencies. The spectral indices are consistent with results presented in Toscano et al. (1998) within the measurement uncertainties, but have much smaller uncertainties because of our better measurements of flux densities. However, compared with Kramer et al. (1999a), the spectral indices show differences clearly larger than the uncertainties. Such discrepancies could be due to flux density measurements biased by scintillation effects, and also the narrower frequency range we are using. We derive a mean spectral index of -1.8 ± 0.1 , which is consistant with previous results and support the idea that MSPs and normal pulsars have similar emission characteristics.

5 POLARIZATION

In Table 4, the fractional linear polarization $\langle L \rangle / S$, the fractional net circular polarization $\langle V \rangle / S$ and the fractional absolute circular polarization $\langle |V| \rangle / S$ averaged over all observations for three bands are presented. The means are taken across the pulse profile. In Fig. 11, 12 and 13, we plot the $\langle L \rangle / S$, $\langle V \rangle / S$ and $\langle |V| \rangle / S$ against frequency for each MSP.

We find the frequency evolution of polarization parameters is different from pulsar to pulsar, and the behaviours are complicated. The fractional linear polarization does not necessarily decrease as the frequency increases, and so does the fractional circular polarization and fractional net circular polarization. This is also no evidence that sources that are highly polarized depolarize rapidly.

REFERENCES

- Bhat N. D. R., Cordes J. M., Camilo F., Nice D. J., Lorimer D. R., 2004, ApJ, 605, 759
- Burgay M. et al., 2013, MNRAS, 433, 259
- Everett J. E., Weisberg J. M., 2001, ApJ, 553, 341
- Gupta Y., Gangadhara R. T., 2003, ApJ, 584, 418
- Han J. L., Manchester R. N., 2001, MNRAS, 320, L35
- Hobbs G. B., Edwards R. T., Manchester R. N., 2006, MNRAS, 369, 655
- Hotan A. W., van Straten W., Manchester R. N., 2004, PASA, 21, 302
- Johnston S. et al., 1993, Nature, 361, 613
- Keith M. J. et al., 2012, MNRAS, 419, 1752
- Keith M. J. et al., 2011, MNRAS, 414, 1292
- Kramer M., 1994, A&AS, 107, 527
- Kramer M., Lange C., Lorimer D. R., Backer D. C., Xilouris K. M., Jessner A., Wielebinski R., 1999a, ApJ, 526, 957
- Kramer M. et al., 1999b, ApJ, 520, 324
- Kramer M., Xilouris K. M., Lorimer D. R., Doroshenko O., Jessner A., Wielebinski R., Wolszczan A., Camilo F., 1998, ApJ, 501, 270
- Lorimer D. R., Kramer M., 2005, Handbook of Pulsar Astronomy. Cambridge University Press
- Lyne A. G., Manchester R. N., 1988, MNRAS, 234, 477
- Manchester R. N., 1995, Journal of Astrophysics and Astronomy, 16, 107
- Manchester R. N., 2008, in American Institute of Physics Conference Series, Vol. 983, 40 Years of Pulsars: Millisecond Pulsars, Magnetars and More, Bassa C., Wang Z., Cumming A., Kaspi V. M., eds., pp. 584–592
- Manchester R. N., Han J. L., 2004, ApJ, 609, 354
- Manchester R. N. et al., 2013, PASA, 30, 17
- Manchester R. N., Hobbs G. B., Teoh A., Hobbs M., 2005, Astron. J., 129, 1993
- Manchester R. N., Johnston S., 1995, ApJL, 441, L65
- Navarro J., Manchester R. N., Sandhu J. S., Kulkarni S. R., Bailes M., 1997, ApJ, 486, 1019
- Ord S. M., van Straten W., Hotan A. W., Bailes M., 2004, MNRAS, 352, 804
- Radhakrishnan V., Cooke D. J., 1969, Astrophys. Lett., 3, 225
- Rankin J. M., 1993, ApJ, 405, 285
- Sotomayor-Beltran C. et al., 2013, A&A, 552, A58
- Stairs I. H., Thorsett S. E., Camilo F., 1999, ApJS, 123, 627
- Thorsett S. E., Stinebring D. R., 1990, ApJ, 361, 644
- Toscano M., Bailes M., Manchester R. N., Sandhu J. S., 1998, ApJ, 506, 863
- van Straten W., Manchester R. N., Johnston S., Reynolds J. E., 2010, PASA, 27, 104
- Yan W. M. et al., 2011a, ApSS, 335, 485
- Yan W. M. et al., 2011b, MNRAS, 414, 2087

Table 3. Flux densities and spectral indices for PPTA MSPs.

PSR	S_{730} (mJy)	$S_{RMS,730}$ (mJy)	S_{1400} (mJy)	$S_{RMS,1400}$ (mJy)	S_{3100} (mJy)	$S_{RMS,3100}$ (mJy)	Spectral index α
J0437–4715	364.3 ± 19.2	255.2	150.2 ± 1.6	42.2	35.6 ± 1.2	20.5	-1.7± 0.1
J0613–0200	6.7 ± 0.3	2.3	2.25 ± 0.03	0.4	0.45 ± 0.01	0.1	-1.90± 0.08
J0711–6830	11.4 ± 1.0	8.5	3.7 ± 0.4	5.7	0.72 ± 0.04	0.4	-1.91± 0.07
J1017–7156	2.5 ± 0.1	0.8	0.99 ± 0.04	0.4	0.21 ± 0.01	0.1	-1.7± 0.1
J1022+1001	14.2 ± 2.8	22.9	4.9 ± 0.4	4.6	1.18 ± 0.03	0.4	-1.73± 0.08
J1024–0719	5.6 ± 0.8	4.9	2.3 ± 0.2	1.7	0.52 ± 0.01	0.1	-1.7± 0.1
J1045–4509	9.2 ± 0.2	1.8	2.74 ± 0.04	0.5	0.48 ± 0.01	0.1	-2.05± 0.06
J1446–4701	±		±		±		±
J1545–4550	±		±		±		±
J1600–3053	2.9 ± 0.1	0.4	2.44 ± 0.04	0.4	0.84 ± 0.02	0.2	-0.9± 0.3
J1603–7202	10.9 ± 0.7	4.9	3.5 ± 0.2	1.7	0.55 ± 0.06	0.4	-2.0± 0.2
J1643–1224	12.4 ± 0.2	1.4	4.68 ± 0.06	0.7	1.18 ± 0.02	0.2	-1.63± 0.03
J1713+0747	10.1 ± 0.8	6.2	9.1 ± 0.7	8.4	2.6 ± 0.2	1.6	-1.0± 0.3
J1730–2304	11.5 ± 0.5	3.9	4.0 ± 0.2	2.0	1.7 ± 0.2	1.5	-1.5± 0.3
J1732–5049	±		±		±		±
J1744–1134	8.0 ± 0.7	5.7	3.2 ± 0.3	3.2	0.77 ± 0.05	0.5	-1.63± 0.07
J1824–2452	11.4 ± 0.5	2.9	2.30 ± 0.05	0.4	0.39 ± 0.01	0.1	-2.3± 0.2
J1832–0836							
J1857+0943	10.4 ± 0.4	3.0	5.1 ± 0.3	2.9	1.2 ± 0.1	0.9	-1.4± 0.2
J1909–3744	4.9 ± 0.3	3.1	2.5 ± 0.2	3.2	0.76 ± 0.04	0.5	-1.29± 0.07
J1939+2134	67.8 ± 2.7	20.9	15.2 ± 0.6	6.2	1.82 ± 0.09	0.9	-2.50± 0.06
J2124–3358	19.3 ± 2.7	17.2	4.5 ± 0.2	2.2	0.82 ± 0.01	0.1	-2.09± 0.05
J2129–5721	5.9 ± 0.5	3.9	1.28 ± 0.09	1.0	0.34 ± 0.05	0.2	-2.1± 0.4
J2145–0750	27.4 ± 3.4	28.5	10.3 ± 1.0	11.2	1.75 ± 0.07	0.8	-2.0± 0.1
J2241–5236	11.9 ± 1.8	16.2	1.95 ± 0.09	1.2	0.35 ± 0.01	0.1	-2.1± 0.2

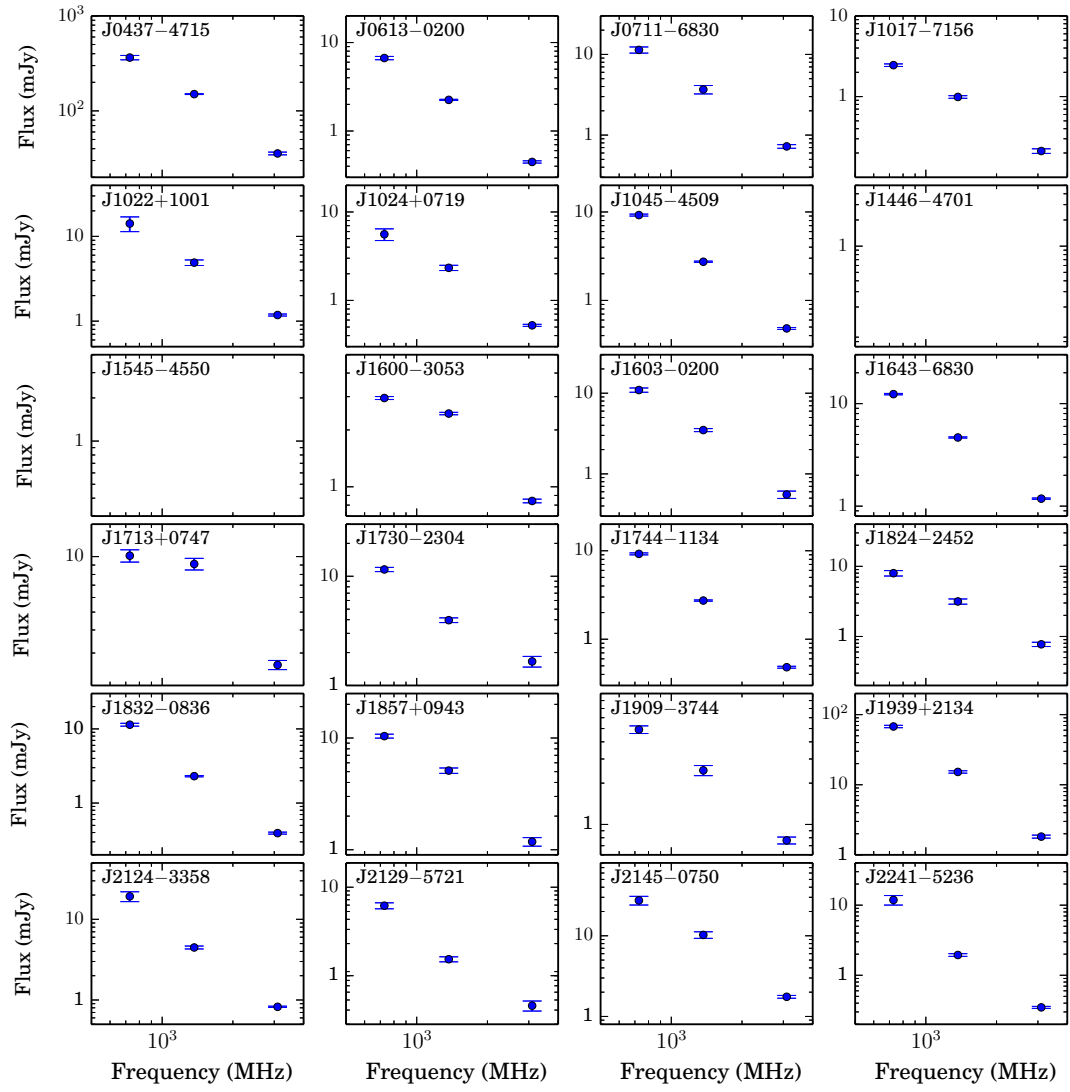
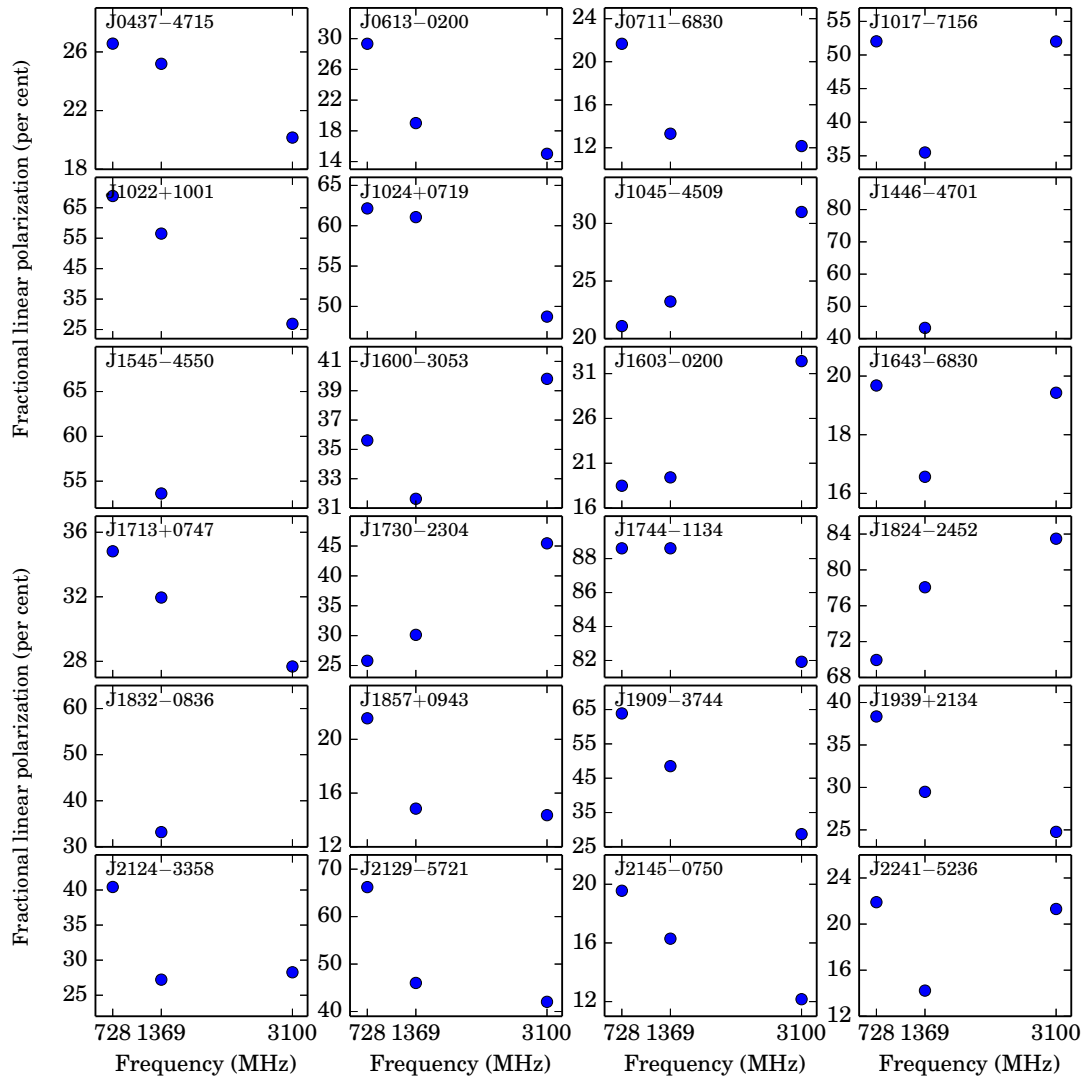
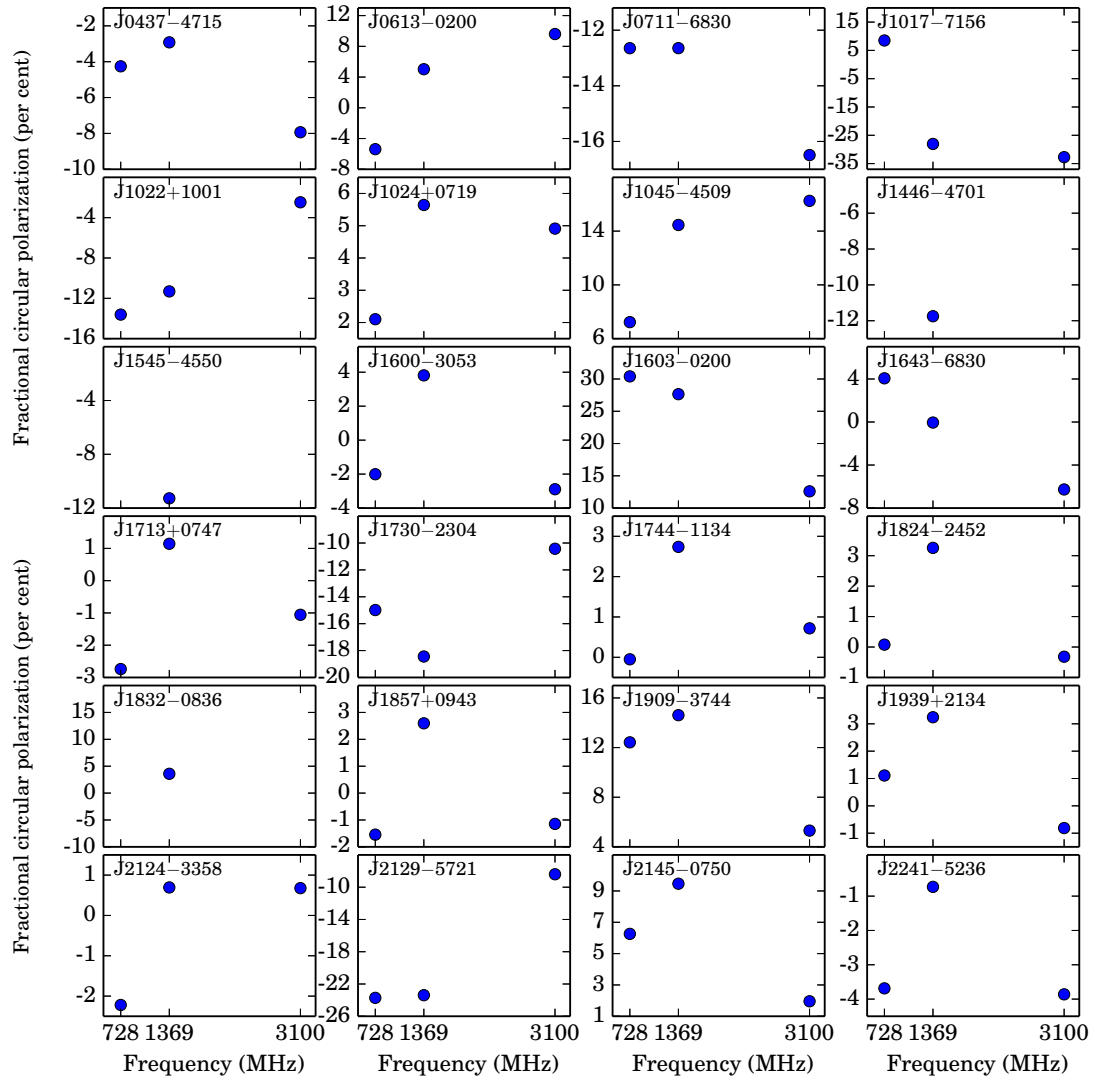
**Figure 10.** Flux density spectra for 24 MSPs

Table 4. Polarization parameters for PPTA MSPs.

PSR	$\langle L \rangle / S$			$\langle V \rangle / S$			$\langle V \rangle / S$		
	730 MHz (per cent)	1400 MHz (per cent)	3100 MHz (per cent)	730 MHz (per cent)	1400 MHz (per cent)	3100 MHz (per cent)	730 MHz (per cent)	1400 MHz (per cent)	3100 MHz (per cent)
J0437–4715	20.2	25.2	26.6	-7.9	-2.9	-4.3	12.3	11.3	15.4
J0613–0200	15.0	19.0	29.3	9.6	5.0	-5.4	13.4	5.7	10.4
J0711–6830	12.2	13.3	21.7	-16.5	-12.6	-12.6	18.3	13.1	13.7
J1017–7156	52.0	35.5	52.0	-32.7	-28.1	8.5	47.7	29.8	28.7
J1022+1001	26.9	56.5	68.9	-2.5	-11.3	-13.6	8.3	13.2	15.1
J1024–0719	48.7	61.1	62.1	4.9	5.6	2.1	11.8	7.1	9.3
J1045–4509	31.0	23.2	21.1	16.3	14.5	7.2	20.1	16.7	12.4
J1446–4701		43.3			-11.7			19.7	
J1545–4550		53.6			-11.3			19.2	
J1600–3053	39.8	31.6	35.6	-2.9	3.8	-2.0	7.4	4.6	14.6
J1603–7202	32.4	19.4	18.5	12.6	27.6	30.4	22.4	31.9	33.4
J1643–1224	19.4	16.6	19.7	-6.3	-0.05	4.1	11.4	13.4	13.8
J1713+0747	27.7	32.0	34.8	-1.1	1.1	-2.7	4.5	4.1	6.4
J1730–2304	45.4	30.1	25.8	-10.4	-18.4	-15.0	17.4	20.9	18.1
J1732–5049									
J1744–1134	81.9	88.6	88.6	0.7	2.7	-0.05	5.2	3.8	5.0
J1824–2452	83.5	78.1	70.0	-0.3	3.3	0.08	10.2	4.4	6.8
J1832–0836		33.2			3.6			15.6	
J1857+0943	14.4	14.8	21.6	-1.1	2.6	-1.5	8.6	6.1	8.7
J1909–3744	28.7	48.5	63.9	5.3	14.6	12.4	8.9	16.4	19.5
J1939+2134	24.8	29.5	38.4	-0.8	3.2	1.1	2.5	3.4	1.7
J2124–3358	28.3	27.2	40.4	0.7	0.7	-2.2	9.3	5.5	4.4
J2129–5721	42.0	46.0	66.2	-8.4	-23.4	-23.7	30.8	26.7	38.1
J2145–0750	12.2	16.3	19.6	2.0	9.5	6.3	9.2	10.3	10.3
J2241–5236	21.3	14.2	21.9	-3.9	-0.7	-3.7	15.8	7.1	7.1

**Figure 11.** The fractional linear polarization of the MSPs.

**Figure 12.** The fractional circular polarization of the MSPs.

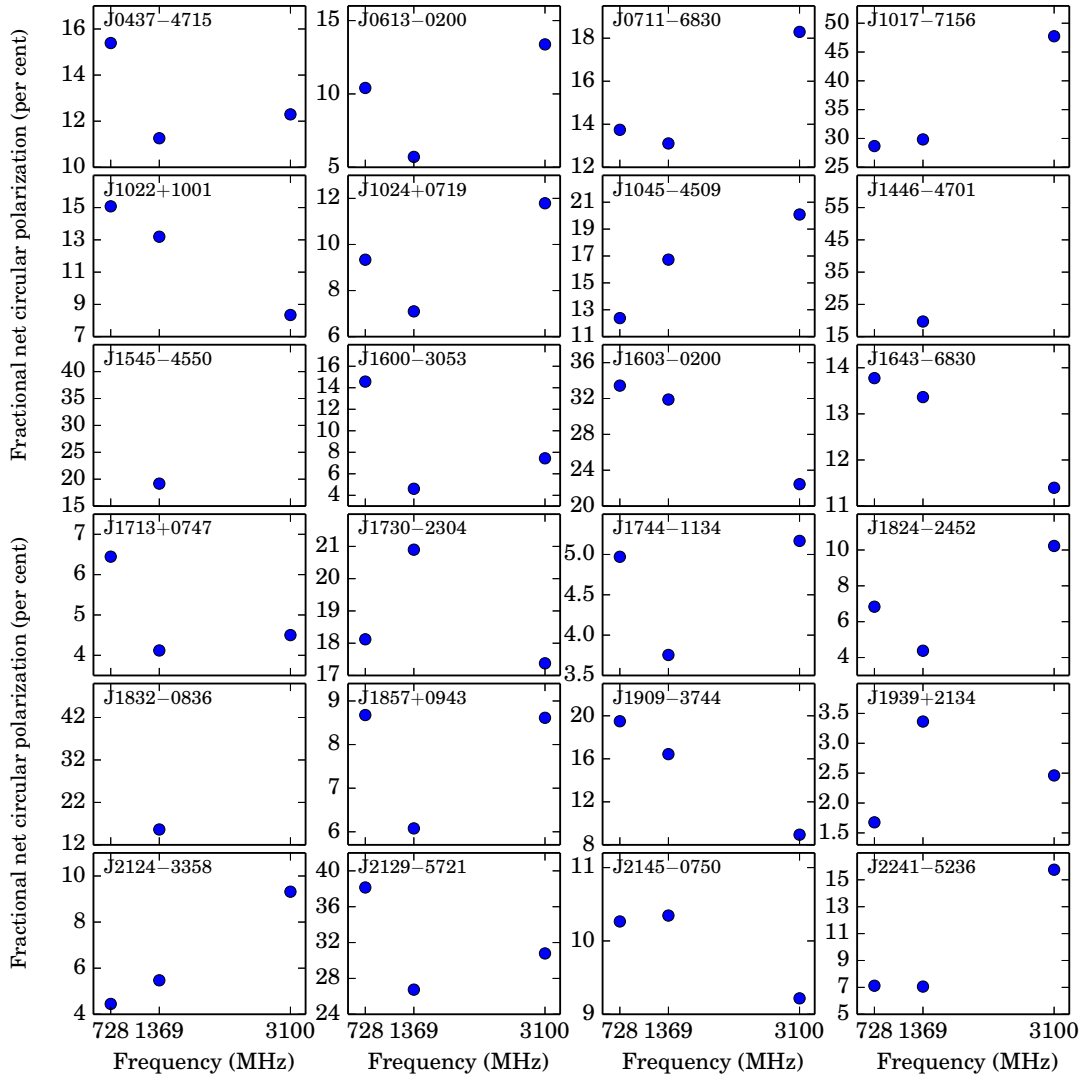


Figure 13. The fractional net circular polarization of the MSPs.